Progress on the CESR Phase III and CLEO III Upgrades at Cornell

Daniel Peterson [a] *

[a] Laboratory of Nuclear Studies, Cornell University, Ithaca, NY 14853 USA

The Cornell Electron Storage Ring (CESR) has embarked on a staged luminosity upgrade program with a goal in excess of 10 fb^{-1} per year. The new focusing scheme at the interaction region will require replacing the CLEO tracking chambers. The CLEO collaboration will take advantage of this rebuilding of the inner detector to improve the capability for high momentum particle identification, while maintaining the excellent charged particle momentum resolution and electromagnetic calorimeter resolution of the present detector.

1. INTRODUCTION

The CLEO II detector [1], installed at the Cornell Electron Storage Ring (CESR), is used for studying the properties of B-meson decays in resonant $\Upsilon(4s)$ production and many aspects of c, τ and $\gamma\gamma$ physics in e^+e^- interactions. Both CESR and CLEO are being upgraded in a staged program over the next 3 years [2]. These upgrades will allow CLEO to take advantage of an integrated luminosity in excess of 10 fb^{-1} per year.

In the final stage of the upgrade, the interaction region optics will severely constrain the space and access available for tracking components. Furthermore, installation of a particle identification device, necessary to provide K-π separation up to 2.8 GeV/c, will limit the tracking components at the outer radius. By integrating the tracking system design and the storage ring interaction region design and installation to limit the scattering material in the tracking volume, the upgraded detector, CLEO III, will provide improved tracking performance in a radially smaller volume.

This paper describes the staged CESR upgrades and the elements of the CLEO III detector, now in construction. Progress in research and development, critical to the completion of the designs for the new detector, is discussed for each element.

*(Presented at "6th Topical Seminar on Experimental Apparatus for Particle Physics and Astropysics, San Miniato, Toscano, 21-24 Maggio, 1996). This work was supported by the U.S. National Science Foundation.

2. CESR

The CESR operations group achieved a luminosity record of 3.2 x $10^{32}cm^{-2}s^{-1}$ in April 1995 with Phase I of the CESR upgrade. In phase I, the beam-beam interactions were reduced by intersecting the electron and positron orbits with a 2.3 mrad crossing angle at the center of the CLEO detector and by electrostatically separating the beams in a pretzel configuration to remove parasitic crossings. New 5-cell, normal copper, RF cavities were installed to replace the aging 14-cell cavities used since 1979. Interaction region vacuum was improved with titanium sublimation pumps to reduce backgrounds in CLEO.

Although a record for storage rings, this luminosity is only a small improvement over previous running because the horizontal β function at the interaction region, shown in Figure 1, was not compatible with the crossing angle beam orbits. In phase I, the maximum in the horizontal β function at 4.3 meters from the interaction region limits the storage ring injection. The beam structure, with 9 *trains* nearly equally spaced at 280 ns, each with 2 bunches having a fine spacing of 28 ns, has the first parasitic crossing near the maximum in the horizontal β function. With insufficient aperture to separate the beams and provide clearance for injection, single bunch current was limited to 9 ma.

2.1. CESR Phase II

The CESR upgrade phase II installation shutdown was complete with the successful beam stor-

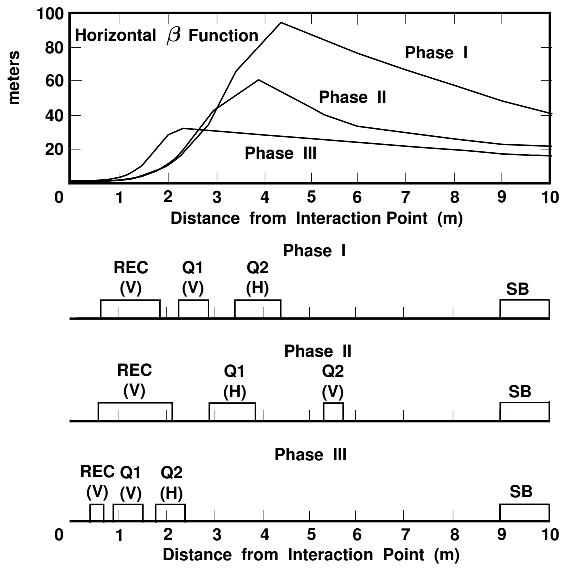

Figure 1. Horizontal β functions and interaction region focusing element configurations for CESR upgrade phases I,II,III. Labels "H" and "V" indicate whether quadrupoles are horizontal and vertical focusing. The location of the first soft-bending magnet is idicated by "SB".

age on October 19, 1995. The major improvement of CESR in Phase II of the upgrade is a modification to the interaction region optics. By increasing the strength of the permanent rare-earth-cobalt (REC) quadrupole and changing the focusing directions of normal copper quadrupole magnets Q1 and Q2, the maximum of the horizontal β function is reduced in magnitude and moved away from the position of the first parasitic crossing. (See Figure 1.) Beam current in Phase II is no longer limited by the ability to inject beam, but rather by the RF cavities. There are four normal copper RF cavities with 5 cells per cavity, first installed during phase I, limiting the single beam current to 300 ma.

Since the start of Phase II operation, the best peak luminosity has been 3.5 x 10^{32}cm^{-2}s^{-1} and the best daily integrated luminosity has been 17.0 pb^{-1}. These values were attained running with only 2 bunches in each of 9 trains as in Phase I and a single beam current of only 150 ma or 8 ma per bunch. The Phase II luminosity is expected to improve to 6.0 x 10^{32}cm^{-2}s^{-1} as the single bunch current is increased to 11 ma (the limit imposed by beam-beam interactions) and the number of bunches per train is increased to 3 (27 bunches per beam) to achieve the RF imposed current limit.

2.2. CESR Phase III

Major improvements of CESR in Phase III of the upgrade are the implementation of four single-cell superconducting niobium RF cavities and a new interaction region optics. This removes the limitation to the current imposed by normal copper RF cavities to allow the highest possible luminosity from a single ring configuration.

A superconducting RF cavity system will allow higher circulating beam currents for several reasons. The impedance to the circulating image current, and therefore the beam, is greatly reduced. Ohmic heating in the cell is eliminated allowing both an increased aperture size and an increased voltage gradient across the aperture. With an increase in the operating voltage, fewer cells are required. The reduction in impedance and number of cells along with the increase in aperture result in a decrease in the coupling to higher order modes which results in an increase in the limit to total beam current.

The Phase III superconducting niobium RF cavities will operate with a voltage gradient of 6 MV/m (1.8 MV/cell) and will allow a single beam current of 500 ma. Since the single bunch current is still limited to 11 ma by the beam-beam interaction, 45 bunches (5 bunches in each of 9 trains with 14 ns spacing) will be required. A prototype of the superconducting niobium RF cavities was successfully tested in CESR at full voltage gradient in August 1994 [3]. The first production cavity will be installed in early 1997 providing experience during phase II operation.

As a result of the increased RF voltage gradient, the bunch length will be reduced to 10 mm. This allows further improvement in the luminosity by reducing β_v^* from the Phase II value of

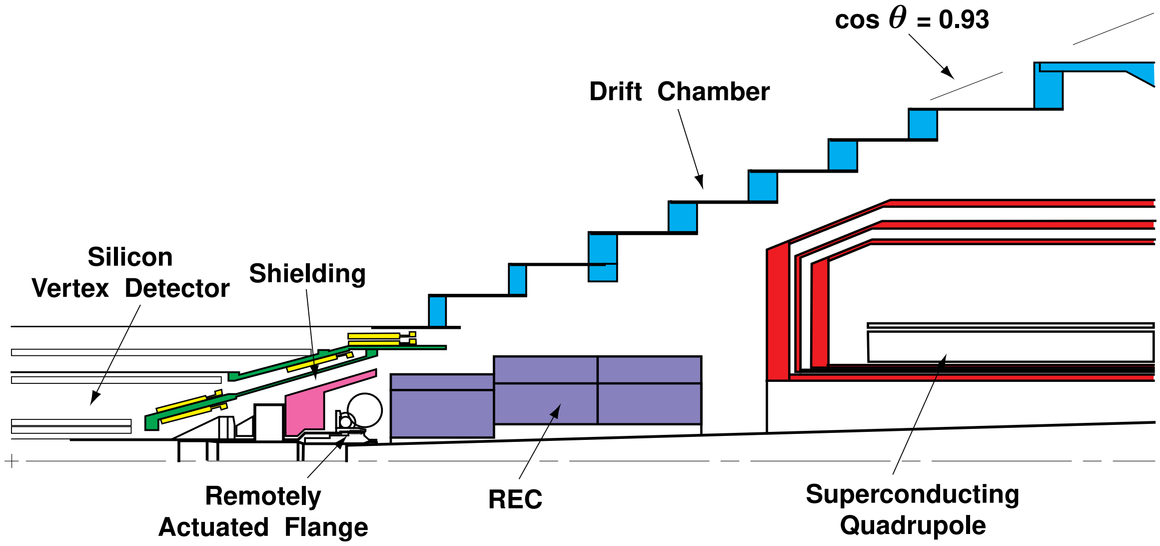

Figure 2. Phase III Interaction Region. Rare-earth-cobalt (REC) and superconducting quadrupoles intrude into the CLEO experiment. The vacuum chamber expands with distance from the interaction point as it passes through the REC. CLEO detector elements are fit into the available volume, $|\cos\theta| \leq 0.93$.

18 mm. The Phase III interaction region is shown in Figure 2. A permanent magnet quadrupole, with a gradient of 30 T/m, is located at 30 cm from the interaction point. This is followed by a pair ofsuperconducting quadrupoles, with gradients of 48 T/m, located at 65 cm from the interaction point. While this configuration of focusing elements achieves a β_v^* is $\leq$10 mm, it must also provide aperture for injection. The horizontal β function, shown in Figure 1, at the first parasitic crossing (which will be at 2.1 m for 14 ns spacing) is further reduced from that of Phase II providing improved injection. The improvements in current and focusing provided by the Phase III upgrade are expected to provide a peak luminosity of 17. x $10^{32}\mathrm{cm}^{-2}\mathrm{s}^{-1}$.

2.3. Compatibility of CLEO with CESR Phase III

The phase III interaction region focusing quadrupoles, as shown in Figure 2, are necessarily physically larger and intrude farther into the CLEO experiment than in Phase II. A new tracking system is required for CLEO to be compatible with the focusing quadrupole. Return magnetic fields are less contained in the superconducting quadrupoles than in the current focusing that uses only permanent magnets. This will require use of a mapping of the magnetic field in the tracking volume for precision momentum measurements of particles at large dip angle.

Beyond placing constraints on the physical dimensions of CLEO components, the focusing magnet elements create an assembly problem. The vacuum chamber through the permanent magnet quadrupole is tapered such that the magnet can not be installed by slipping it over the vacuum chamber after connections to the interaction region vacuum chamber have been completed. A permanent assembly tube, (containing and supporting the preassembled inner elements: vertex detector, permanent magnet elements, interaction region vacuum chamber) is not acceptable because the added material would degrade the tracking resolution. Furthermore, an assembly process requiring access to a flange (connecting a permanent magnet section of the vacuum chamber to an interaction point section) is also unacceptable because it would greatly compromise the remaining solid angle coverage of the tracking system. Assembly of the CESR Phase III interaction region is planned to utilize a remotely actuated flange shown in Figure 2. Prototypes of this flange have been successfully demonstrated. This procedure replaces the earlier described procedure [4] to utilize a removable insertion tube.

3. CLEO III Tracking

In addition to the constraints imposed by the CESR Phase III interaction region focusing magnets, the outer radius of the CLEO III tracking system is limited to less than 82 cm to provide space for a ring imaging Cerenkov (RICH) particle identification system. Physics goals require that the momentum resolution of the CLEO II tracking system (with outer radius of 95 cm) be maintained in the CLEO III tracking system. This criteria can be met with a silicon strip vertex detector having a spatial resolution of 40 μm and a drift chamber with spatial resolution comparable to the current CLEO II drift chamber provided that a gas with radiation length $\geq$330 m is used and scattering material between the outermost silicon layer and the innermost drift chamber layer is limited to 0.15% radiation length. By offsetting an increase in the spatial resolution component with a decrease in the multiple scattering component, CLEO III tracking resolution is better than that of CLEO II throughout the momentum range relevant for a symmetric energy storage ring: up to 2.8 GeV/c [4].

3.1. SILICON VERTEX DETECTOR

A silicon strip detector will be utilized in CLEO III to make precision measurements for use as part of the momentum measurement as well as for measuring vertex positions. This detector design is an evolution of the CLEO II silicon vertex detector [5]. Experience with that detector, in operation since December 1995, shows that improvements can be made by reducing excess capacitance, excess noise, and complexity of design.

The CLEO III silicon detector will be made of double sided strip detectors arranged in 4 cylindrical layers with radii shown in Table 1. Silicon detectors of a single design will be used in all layers to simplify the design. Each detector is 300 μm thick and has double sided strip readout: 511 r-ϕ-measuring strips with 50 μm pitch and 511 z-measuring strips with 100 μm pitch. The detectorss within each layer are mounted in rigid azimuthal sections with each section requiring several detectors to make up the required length as enumerated under “sections” and “detectors” in the table. The azimuthal sections are dynamically mounted to rigid end cones which are, in turn, rigidly mounted to each other through a carbon fiber tube that is between the 3rd and 4th layers.

Table 1
CLEO III Silicon Vertex Detector Parameters

layer	radius (cm)	sections	detectors
1	2.50	7	3
2	3.75	10	4
3	7.00	18	7
4	10.0	26	10

Excess capacitance is a problem in the CLEO II silicon detector. The source of this capacitance is the double metal readout in which an array of longitudinal readout *traces* are placed over the z-measuring *strips* to avoid the extra material involved in using direct mounted flex circuits. Each readout trace has ohmic connection to one strip but is capacitively coupled to 510 strips, and (through the strip to which it is connected) capacitively coupled to another 510 readout traces. Coupling capacitance is large in the CLEO II detector because the z-measuring side is the n-type side which suffers from the effective increase in the width of the strips due to a charge layer that develops around the n-type implant in a weaker n-type substrate. In CLEO III, the z-measuring side is chosen to be the p-type side to minimize the capacitive coupling. Measurements of the test pieces verify that, with the narrow p-implant strips, the parallel plate model of capacitance is not applicable; capacitance is weakly dependent on trace-strip spacing and linearly dependent on the widths. The capacitance can be slightly reduced by narrowing the strips and traces in the regions of the overlaps but there is no advantage to a costly increase in the oxide thickness. Strips will be 10 mm wide, traces will 8 mm wide, and the oxide thickness will be 3 μm to reduce the capacitance to $\leq$10 pF per detector strip.

Readout traces on the z-measuring sides of detectors within each half of the azimuthal sections will be dc coupled to form a common readout. Thus, as many as 5 detectors will be connected in parallel causing system noise to be sensitive to the individual detector strip capacitance. Noise levels from many sources, including overlap capacitance, have been evaluated and a prediction made of the noise charge as it depends on the number of detectors. Measurements made on prototype azimuthal sections, shown compared to the prediction in Figure 3, indicate that the overlap capacitance is the dominant noise source and that noise can be limited to 900 e/detector on the z-measuring side.

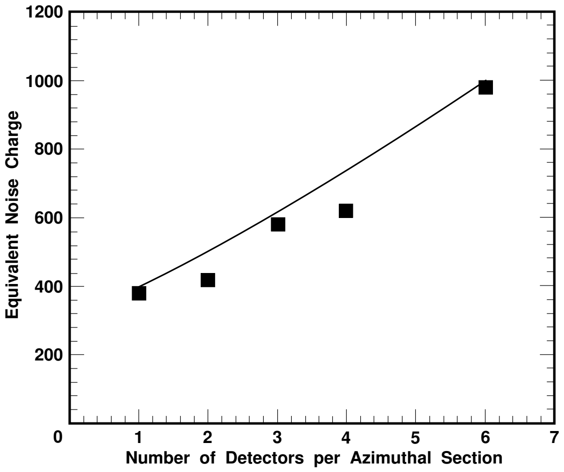

Figure 3. Noise measured in prototype azimuthal sections of p-type detectors vs. number of detectors connected in parallel. Measurements from test fixtures are shown as squares. The line is a prediction based on all known noise sources.

The r-ϕ-measuring strips of the CLEO III detectors will be on the n-type implant side and require p-type implant barriers to avoid ohmic interconnection of the strips in an n-type substrate. In CLEO II, where the z-measuring strips are on the n-type side, the n-type strips suffer from noise that is in excess of what can be accounted for by the bias resistor and trace resistance. In that case, the p-type implant barriers are of the "common" design as shown in Figure 4. A SPICE

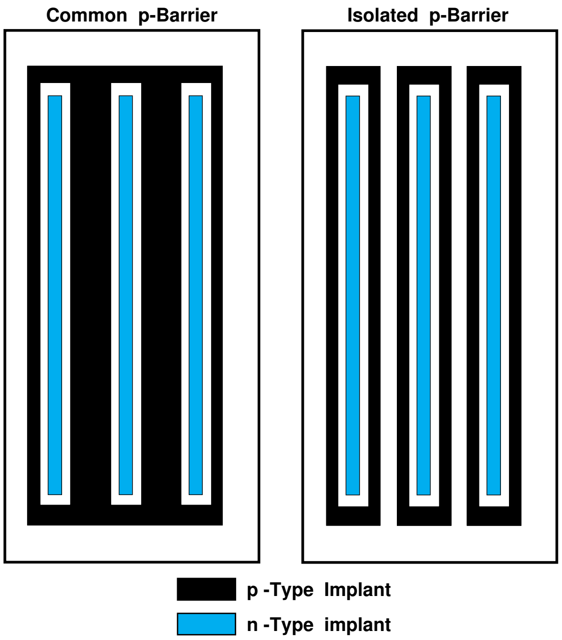

Figure 4. P-type implant barrier configurations for the CLEO II "common" and the CLEO III "isolated" designs.

model of distributed capacitance and resistance in the common p-type barrier, as shown in Figure 5, duplicated the observed noise. Further simulation showed that the noise can be greatly reduced by removing the ground loops in the "common" design by either eliminating the conducting paths of the "end" resistors or the "joining" resistors

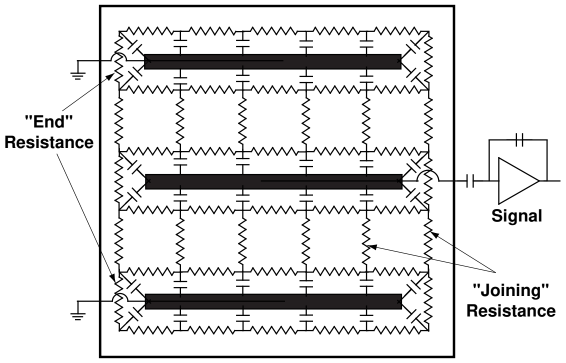

Figure 5. Schematic of capacitance and resistance in SPICE model of the “common” p-type barrier design.

shown in the figure. These calculations were confirmed with measurements of test structure detectorss of several p-type barrier designs. The CLEO III detector will be manufactured with p-type barrier of the “isolated” design, as shown in Figure 5, effectively cutting the “joining” resistors as shown in Figure 4. Further study showed that, since the source of the noise is resistance in the p-type barrier itself, the noise can be further reduced by metalizing the surface of the barrier thereby shorting the resistance. Feasibility of the metalization is being investigated. Noise is expected to be reduced to $\leq$200 electrons/detector.

Capacitance on the n-type implant side can be reduced by clearing the electrons from the Si-SiO_2 interface. This is achieved by biasing the p-type barrier voltage below the bias voltage of the n-type implant. Measurements of test structures indicate that the capacitance on the n-type side can be reduced to $\leq$10 pF per detector strip.

Finally, capacitive noise will be minimized by using a long integration time (1 to 3 μs) to reduce the amplifier noise slope to $\leq$10 e/pF. This corresponds to up to 54 crossings but simulations of photon and particle noise in the detector indicate that a strip occupancy of $\sim$.1%/μs can be expected.

This silicon detector research on test structures ordered in 1994 and 1995 have shown that significant improvements can be made in the signal-to-noise ratio. Orders for the final design detectors will be made in August 1996.

3.2. DRIFT CHAMBER

The drift chamber endplate is made of two sections as shown in Figure 6. This design allows satisfying (sometimes conflicting) requirements placed on the mechanical design of the endplate: the intrusion of the CESR Phase III focusing magnets, the need to provide mechanical space for CLEO III particle identification, the need to minimize radiating material blocking the endcap electromagnetic calorimeter, and the specification of a maximum of 0.15% RL scattering material separating the active volume from the last silicon measurement.

The smaller radius section of the drift chamber endplate is made of a set of 8 aluminum rings interconnected with nonmagnetic steel bands via radial screws. With a highly tapered shape, this section of the endplate provides the maximum use of the available tracking volume; charged particles will be measured within $|\cos\theta| \leq 0.93$. The rings design was chosen over a monolithic inner section design to aid in the drilling of wire holes. Holes within a ring will be precision aligned to 75 μm and individually surveyed to 25 μm . Ring-to-ring alignment will be measured optically and verified by minimization of errors of high momentum tracks.

The outer endplate section is machined from 16.5 cm thick aluminum plate. Although the surface is terraced to allow flat surfaces for drilling and wire holding devices, the general shape is conic with thickness 1.55 cm and sagitta 7.6 cm. Stiffness is increased with an integral outer support ring and by constraining the angular deflection at the inner radius.

This design not only provides a substantial reduction in scattering material but provides the stiffness required to support the thin inner gas seal. Stable mounting of the inner gas seal requires that the endplates not move under the dynamic loads of either handling during installation or the changing load due to creep in the aluminum field wires. Calculations using an ANSYS model

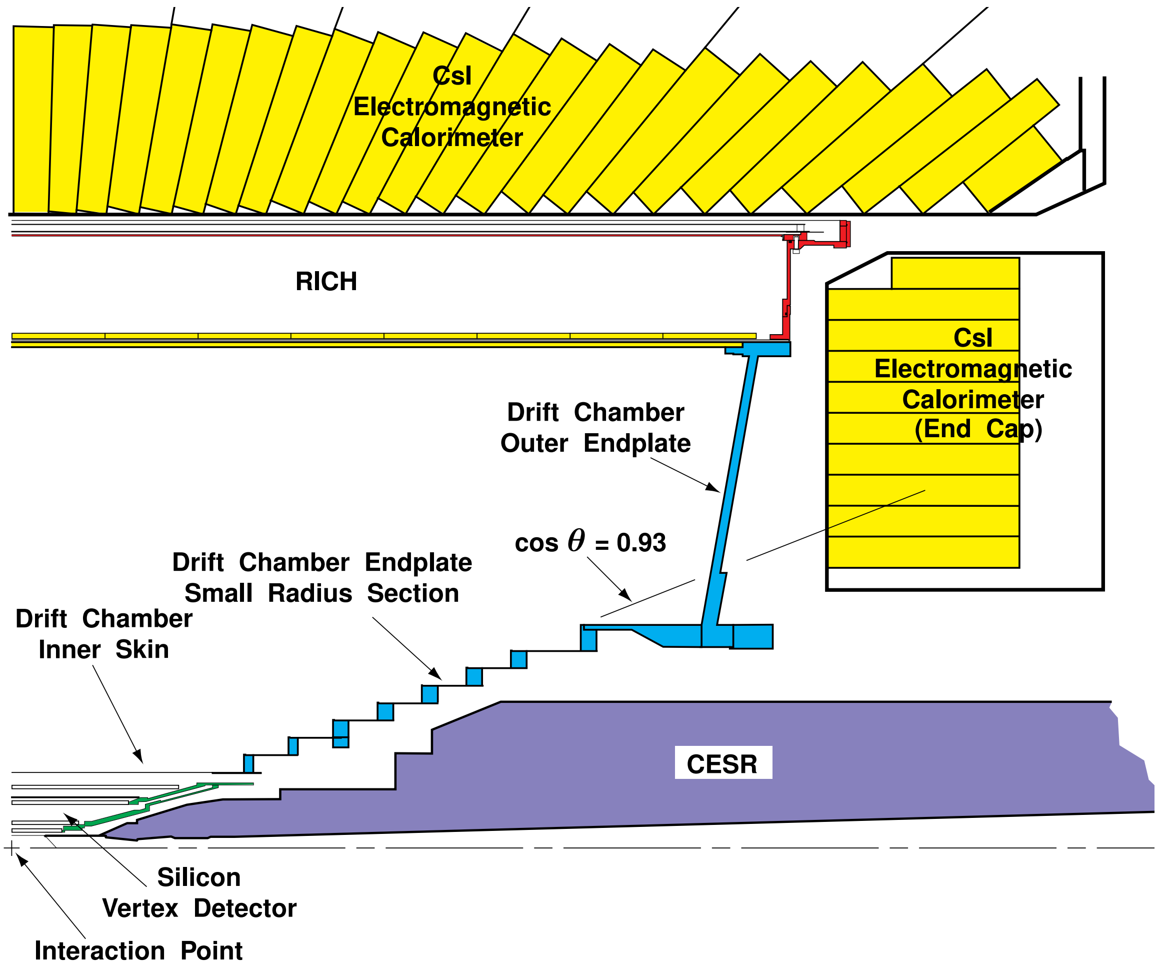

Figure 6. CLEO III quarter section. The superconducting solenoidal magnet coil and muon detection are not shown. More details of the CESR components are shown in Figure 2. The RICH particle identification is shown in Figure 9.

show that motions due to applied forces are small compared to the strain that can be tolerated by the inner tube. The effect of wire load on the endplate was also modeled resulting in a deflection of only 1.0 mm while the current CLEO II endplate (3.2 mm flat aluminum) deflects 9.4 mm. Since the endplate deflection is much less than the wire strain ($\sim$7 mm) aluminum field wires will creep with nearly constant strain, rather than constant tension, resulting in a stable endplate deflection. In contrast, the condition of creep with constant strain is attained in the case of the CLEO II drift chamber only by the use of a rigid inner tube, a condition that is not possible in CLEO III.

The thin inner skin will be made from 2.0 mm expanded acrylic with 20 μm aluminum skins which provide a gas seal and RF shielding. The tube will be mounted to the endplate with strain absorbing joints which provide sufficient position accuracy to avoid distortion of the electric field of the inner drift cell layer.

Drift cells will be "square" with 3 field wires per sense wire and a 7 mm half cell size (maximum drift distance). Experience in the CLEO II drift chamber and simulations indicate that there is no advantage to hexagonal cells and only minor advantage to a cell cage with more field wires. Furthermore, alternate field cage designs are not compatible with the assembly method used for the inner section.

Longitudinal measurements will be made with a segmented cathode readout on the last layer and stereo wires. Transitions between layers with different stereo angle present a problem in the chamber design. If the chamber is built with double field wire layers at the interfaces between layers with different stereo angle the number of points measured along the tracks would be decreased. The alternative is to share common field wire layers between layers with different stereo angle. In this case one or both of the layers has a field cage with non-constant radial distance or azimuthal relation to the field wires which would distortions in the time-to-distance relation. These longitudinally dependent distortions are particularly difficult to calibrate and, therefore, lead to a degradation of the spatial resolution. In the CLEO II drift chamber, the variation in the azimuthal relation to the field wires is insignificant while the affect of the non-constant radial distance is to cause 20% changes in the drift time.

To eliminate the interfaces with non-constant radial distance in the CLEO III drift chamber, there will be only one axial-to-stereo transition where separate field wire layers will be used. The inner section will thus be axial to improve very low momentum pattern recognition. The outer section will be all stereo with sets of 4 layers (for local ambiguity resolution) strung with almost equal stereo angle but precisely parallel in azimuth. Sequential groups of 4 layers will alternate in sign of the stereo angle while the magnitude of the stereo angle will be adjusted to maintain radial separation of the layers constant to within 77 μm . To maximize the number of measurement points there are common field wire layers at the interfaces of stereo layers such that one in four layers has a non-constant azimuthal relation to the field wires on one side.

Use of a helium based chamber gas mixture is necessary to meet the requirement of a radiation length $\geq$330 m and, therefore, meet the momentum resolution requirements of CLEO III. The choice of gas mixture is complicated by the 1.5 Tesla CLEO magnetic field. In this magnetic field, Ar-C_2H_6 (50-50), used in CLEO drift chambers since 1978, suffers a significant loss in efficiency at drift distances greater than 5 mm in a 7 mm (maximum drift distance) cell operating at 2000 V. To ensure that a long radiation length gas mixture could be identified that did not suffer even greater performance degradation at 1.5 Tesla, efficiency and spatial resolution of candidate gas mixtures were measured using cosmic rays in test chambers mounted within the CLEO experiment magnetic field and operated during normal data taking. The test chambers had 7 mm (maximum drift distance) cells and were operated at the voltage required to provide an average pulse height equivalent to that observed for Ar-C_2H_6 (50-50) at 2000 V. Hit efficiencies for Ar-C_2H_6 (50-50) and He-C_3H_8 (60-40) are shown in Figure 7. Efficiency loss is observed in the Ar-C_2H_6 mixture that is similar to that expected from experience with the CLEO II drift chamber. Hit efficiency is improved with the use

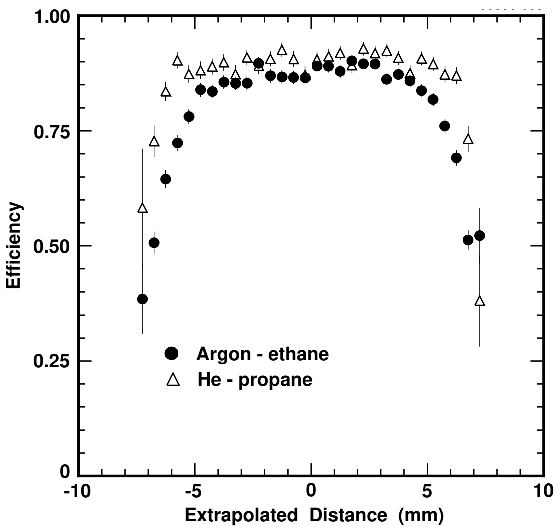

Figure 7. Hit efficiency for a helium based drift chamber gas. Efficiency is measured for hits on tracks in a 7 mm drift cell in a 1.5 T magnetic field.

of He-C_3H_8 (60-40). Similar improvement was observed for He-C_2H_6 (50-50), He-C_3H_8 (40-60), and He-C_4H_{10} (70-30) gas mixtures. In the same study, spatial resolution for He-C_3H_8 (60-40) improved to 102 μm in the central part of the cell as compared to 138 μm observed for Ar-C_2H_6 (50-50). Measurements of helium based gas mixtures at zero magnetic field also show improved spatial resolution and similar total ionization resolution [6].

Aging in chambers using He-C_3H_8 (60-40) and He-C_4H_{10} (70-30) gas mixtures was measured using an Fe^{55} source to expose chamber wires to a large charge. For comparison, it is estimated that the CLEO II drift chamber wires have been exposed to $\leq$8 milliCoulombs/cm in 10 years of operation. Test chamber wires were exposed to 100 milliCoulombs/cm with an observed loss in pulse height of 4% in Ar-C_2H_6 (50-50) and a similar or smaller loss in either of the helium based mixtures. The results of the aging and performance studies were so encouraging that the CLEO II drift chamber gas mixture was changed to He-C_3H_8 (60-40) for the CESR Phase II running beginning in 1995.

Problems associated with the aluminum field wire and wire mounting, encountered in the CLEO II drift chamber, must be solved before the CLEO III drift chamber, with limited accessibility to the inner layers, can be installed. There have been 55 broken field wires (out of 36000) in 10 years of operation. In the same time period, there have been 200 sense wire HV feed-through failures, or 1% of the 24000 feed-throughs (2 per wire) operating at +2000V.

Wire breaking has been solved by making two changes, either of which will separately solve the problem. First, the available wire is much stronger. The CLEO III drift chamber will be constructed with 110 μm aluminum 5056, gold plated wire as was the CLEO II drift chamber. (Gold plating is reduced to .75 μm to reduce scattering.) While wire is typically installed with 180 grams tension, the currently available wire has a breaking strength of at least 470 grams, compared to 300 grams for the wire used in the earlier chamber. Secondly, the wire holding method is modified. The high voltage feed-through and crimp pin to be used in the CLEO III drift chamber are shown in Figure 8. The wire is ultimately

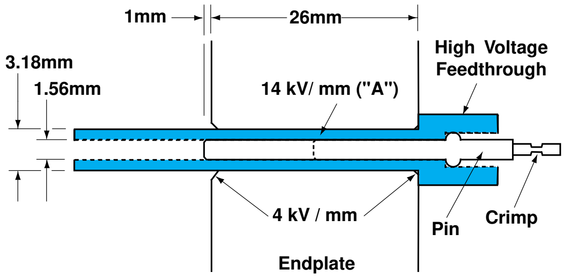

Figure 8. CLEO III drift chamber high voltage feed-through and crimp pin. The metal crimp pin will extend through the endplate. CLEO II crimp pins extended partially through the endplate as indicated by point “A”.

held by a crimp as shown in the figure. In the CLEO II drift chamber the pin is similar but the core (where the crimp is made) is copper and, therefore, harder than the aluminum wire. This condition results in the wire being deformed at the crimp. Small variations in the crimping can yield significant changes in the wire cross section at the crimp causing the yield strength to be exceeded. In the CLEO III drift chamber, the core is changed to an aluminum alloy that is softer than the aluminum wire even when work hardened. The core then flows around the wire at the crimp without deforming the wire.

Breakdown of the high voltage feed-throughs will be reduced by a modification to the crimp pin length. In CLEO II, the crimp pin ends at position “A” as shown in Figure 8. An electrostatics model of the CLEO II pin geometry shows that the electric field is 14 kV/mm at the pin end even with the pin end edges chamfered. This is the location of all feed-through breakdowns. Although electric field is considerably lower than the specification breakdown voltage for the injection molded plastic material, imperfections in the molding or strain due to dimensional piece-to-piece variations in the feed-throughs, crimp pins or holes has lowered the breakdown voltage. There has been no bushing breakdowns in the stereo wires in CLEO II which use the same feed-through with a longer pin which extends beyond the endplate. In CLEO III, the pin will be lengthened to extend beyond the endplate surface, as in the case of CLEO II stereo wires, and the drilled holes will be chamfered to reduce the electric field to $\leq$4 kV/mm at all positions.

4. CLEO III Ring Imaging Cerenkov Particle Identification

A ring imaging Cerenkov detector (RICH) will be installed between the radii of 82 cm and 94 cm, between the drift chamber and existing CLEO II CsI electromagnetic as shown in Figure 9. The LiF crystal radiator provides a Cerenkov angle of 48^o for a 2.8 GeV/c π. The expansion volume is highly purified nitrogen. The separation window is CaF_2 which is chosen to not only be ultraviolet transmitting but also stable in the MWPC gas.

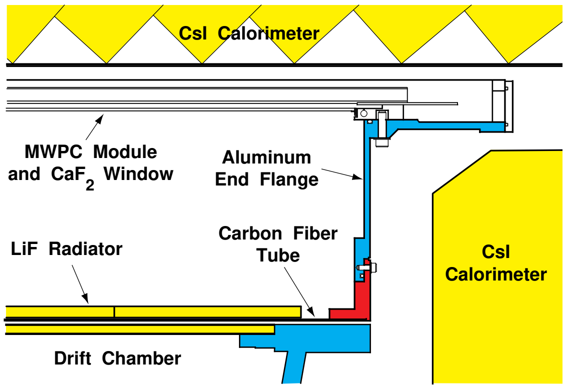

Figure 9. Schematic of the RICH as installed in CLEO III between the drift chamber and the CsI electromagnetic calorimeter.

The MWPC gas is triethylamine (TEA) and CH_4 which has a short UV photon conversion length. Images of the Cerenkov counter rings are observed with 230000 1 cm^2 cathode pads of the MWPC.

The mechanical structure is a carbon fiber tube with aluminum end flanges that supports all of the radiators. MWPC modules, including the separation window which supports the uninstrumented side of the cathode, are attached to the tube structure by strain relieving longitudinal ribs to prevent the development of leaks between the TEA and the expansion volume gas. Although the radiator and the MWPC modules are segmented, the expansion volume is unobstructed because the Cerenkov light cone will spread over multiple MWPC modules.

Cosmic ray test results, with a single MWPC module, indicate that the modules can detect 13 photoelectrons per charge particle when charge particles are incident on the radiator at 30^o to the normal. Figure 10 shows a calculation of the number of photoelectrons expected as a function of $|\cos\theta|$ where θ is the angle of incidence relative to the surface of the radiator (or the track polar angle for a radiator mounted parallel to the beam line). The calculation for a plane radiator agrees well with the measurement

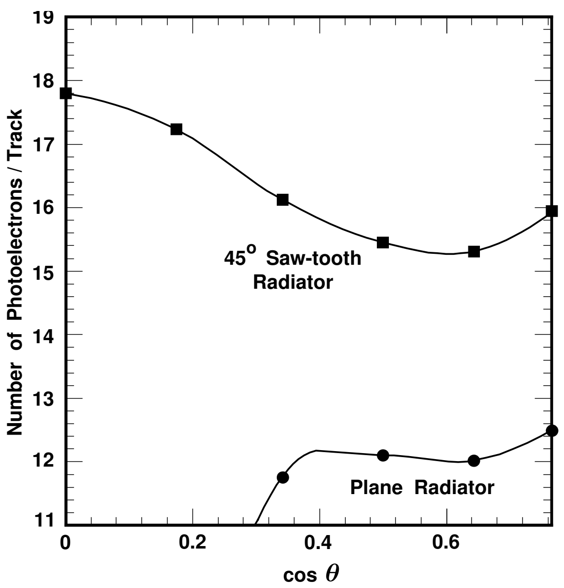

Figure 10. Calculated RICH response for two radiator geometries. The efficiency for a plane radiator is zero at normal incidence.

at $|\cos\theta|$ =0.5 but shows that, for particles incident with $|\cos\theta|$ <0.35, the efficiency will be degraded. Since the Cerenkov angle is close to the angle of internal reflection, the efficiency is greatly reduced at small angle of incidence. Efficiency can be regained by tilting the individual radiator crystals, thereby increasing the angle of particle incidence. Resolution would be compromised, though, because the resulting variation in the expansion distance complicates the calibration in that the image radius would be a function of the Cerenkov angle and the longitudinal position of incidence. At edges of radiator crystals Cerenkov radiation can be scattered by neighboring crystals. Most importantly, use of this method degrades the possible resolution of a RICH counter installed in limited radial space because the expansion distance can be greatly reduced at ends of radiator crystals.

An alternative is the *saw-tooth* radiator design (shown in Figure 11) where total internal reflection is avoided by tilting the radiator surface locally rather than tilting the entire radiator crystal. The grooves are cut longitudinally, providing

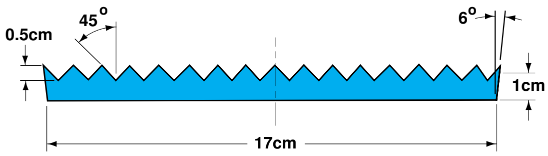

Figure 11. End view of the saw-toothed radiator design. The grooves are oriented parallel to the beam line.

an exit surface that does not change with longitudinal position. In contrast to the tilted radiator design the expansion distance is constant to within 0.5 cm. Photoelectron collection is then improved at all angles of particle incidence as shown Figure 10 where results are shown for a calculation of the light collection from a radiator with surfaces cut 45^o from the normal. The resulting image is complicated. Figure 12 shows the shape of this image for many events although one event would have the photon intensity shown in Figure 10. Mirror-image central arcs come from azimuthally opposite sides of the Cerenkov cone. Outer arcs are due to photons that exit the radiator after one total internal reflection. Surface polishing is potential problem in the saw-tooth radiator design but early tests yield >95% transmission relative to a simple 45^o prism. Light leaks, due to imperfect polishing on otherwise totally internally reflecting surfaces are <5%. The leaks are a source of background to the expected image pattern and are due to imperfections in the polishing. Refinements in the polishing technique are expected to reduce the leaks. Although pattern recognition is complicated, the saw-toothed radiator design has been chosen to be the desirable solution over the tilted radiator design.

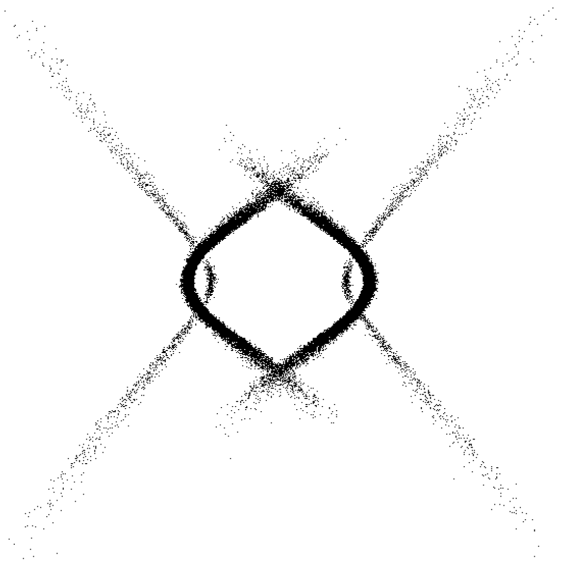

Figure 12. Cerenkov light image of the saw-toothed radiator design.

5. CONCLUSION

The research that is required to complete the designs of each of the new detector elements has been successful. In the case of the silicon vertex detector, capacitance has been reduced to less than 10 pf/detector on both the p-type and n-type sides. Excess detector noise associated with the p-type barriers on the n-type side has been minimized. In the case of the drift chamber, a helium based gas has been demonstrated to provide improved efficiency and resolution in a 1.5 T magnetic field. Broken wire and HV failure problems of the current chamber have been solved. The endplate design places less material before the endcap calorimeter yet is rigid enough to allow mounting a fragile, low mass, inner gas seal. In the case of the ring imaging Cerenkov detector, a solution has been found for the problem of total internal reflection at small polar angle.

The storage ring upgrade and new detector elements are now entering the construction phase. Construction of the superconducting quadrupole magnets was ordered May 1996 for delivery in January 1998. The first of the superconducting RF cavities will be installed in early 1997 and construction of the remaining 3 cavities is ordered. The silicon detector detector design is final and the detectors were ordered in August 1996. Drift chamber endplates were ordered in Setember 1995 with delivery expected February 1997. Delivery of the wire, crimp pins and feed-throughs are expected to be complete at that time as well. The LiF crystal ingots for the ring imaging Cerenkov detector are to be delivered February 1997. Assembly of the detectors is to be completed in time for installation in March 1998.

New components of the CLEO III detector will provide charged particle momentum resolution, vertex reconstruction, and K-π separation up to 2.8 GeV/c. The excellent electromagnetic calorimetry provided by the CLEO II cesium iodide crystal array will be retained. The CLEO III detector will take advantage of an integrated luminosity in excess of 10 fb^{-1} per year. By the year 2002, the total luminosity provided by CESR to CLEO II and CLEO III, is projected to be 62 fb^{-1}[7].

REFERENCES

1. Y. Kubota *et al.*, Nucl. Inst. and Meth. A320 (1992) 66-113.
2. The CESR/CLEO Upgrade Project, CESR and CLEO Staff, Cornell Laboratory of Nuclear Studies preprint CLNS 93/1265 (1993).
3. R. S. Galik, Nuclear Physics B (Proc Suppl.) 50 (1996) 280-287.
4. D. Peterson, Nucl. Inst. and Meth. A360 (1995) 263-266.
5. J. P. Alexander *et al.*, Nucl. Inst. and Meth. A326 (1993) 243.
6. K. K. Gan *et al.*, Nucl. Inst. and Meth. A374 (1996) 27-33.
7. The CESR-CLEO Program, Karl Berkelman, Cornell Laboratory of Nuclear Studies preprint CLNS 96/1398 (1996).